1991

Electrode Kinetics of Oxygen Reduction in Lithium Carbonate Melt: Use of Impedance Analysis and Cyclic Voltammetric Techniques to Determine the Effects of Partial Pressure of Oxygen

Bhasker B. Davé
Texas A & M University - College Station

Ralph E. White
University of South Carolina - Columbia, white@cec.sc.edu

Supramanian Srinivasan
Texas A & M University - College Station

A. John Appleby
Texas A & M University - College Station

Publication Info

Journal of the Electrochemical Society, 1991, pages 673-678.

DOI: 10.1149/1.2085656
http://dx.doi.org/10.1149/1.2085656

Electrode Kinetics of Oxygen Reduction in Lithium Carbonate Melt: Use of Impedance Analysis and Cyclic Voltammetric Techniques to Determine the Effects of Partial Pressure of Oxygen

Bhasker B. Davé* and Ralph E. White**

Center for Electrochemical Engineering, Department of Chemical Engineering, Texas A&M University, College Station, Texas 77843

Supramanian Srinivasan and A. John Appleby****

Center for Electrochemical Systems and Hydrogen Research, Texas Engineering Experiment Station, Texas A&M University, College Station, Texas 77843

ABSTRACT

The effects of the partial pressure of oxygen and temperature on the oxygen reduction on a submerged gold electrode in a lithium carbonate melt were investigated using cyclic voltammetry and impedance analysis. The values for the mass-transfer parameters, $D_O^{1/2}C_O$, obtained from cyclic voltammetry and impedance analysis were in good agreement. The reaction orders for oxygen at 800°C were calculated to be about 0.3 for the exchange current density and 0.5 for the product $D_O^{1/2}C_O$; these values are consistent with the mechanism proposed in the literature for oxygen reduction in Li_2CO_3 melt.

An elucidation of the oxygen reduction reaction in molten alkali carbonate is essential because overpotential losses in the molten carbonate fuel cell are considerably greater at the oxygen cathode than at the hydrogen anode. Appleby and Nicholson (1-4) examined the oxygen reduction reaction in molten carbonates on a submerged gold electrode using steady-state and potential scan techniques. They observed that oxygen dissolves chemically in molten carbonate as peroxide and/or superoxide ions depending on the cations present in the melt. In pure Li_2CO_3 or a Li-rich melt the peroxide species is dominant, whereas in a K-rich melt the superoxide species is dominant. Hence, the oxygen reduction mechanism strongly depends on the cations present in the melt. Lu (5) investigated the oxygen reduction process in pure Li_2CO_3 and a Li-K (62 mole percent (m/o):38 m/o) carbonate eutectic mixture using a potential step method. The exchange current density, determined by Lu (39 mA/cm^2 for 90% O_2 and 10% CO_2 at 750°C in Li_2CO_3 melt), is two orders of magnitude higher than that observed by Appleby and Nicholson (0.34 mA/cm^2) who used the potential scan technique. Lu concluded that the exchange current densities determined from the potential scan data underestimate the actual values. Uchida *et al.* (6-8) determined the kinetic parameters of oxygen reduction in a Li-K (42.7 m/o:57.3 m/o) carbonate eutectic melt on a gold electrode using impedance analysis, potential step, and coulostatic relaxation methods. They found that the exchange current density was about the same order of magnitude as that observed by Lu. In addition, they concluded that impedance analysis is the most reliable of the three methods for the determination of the kinetic parameters for oxygen reduction in molten carbonates. These studies make it clear that the mechanism for the oxygen reduction in molten carbonate is not well understood. Consequently in the present work, the kinetic and transport parameters are determined as a function of P_{O_2} and temperature using cyclic voltammetry and impedance analysis.

Experimental

The experimental arrangement and the electrochemical cell assembly used here have been described elsewhere (9). The working electrode was made of a submerged gold flag (0.025 mm thick), with a geometrical area of 1 cm^2, connected to the gold current collector (0.5 mm diam) by a thin gold wire to minimize the meniscus effect (10). The counterelectrode consisted of a large gold foil which was used as an inner liner of the cell to ensure uniform current distribution. The reference electrode was also made of a gold foil, but encased in an alumina tube which was pressed against the bottom of the electrochemical cell. The high purity (99.9%) gold foils and wires were obtained from Johnson Matthey/ÆSAR Group. Digital mass flow controllers/meters manufactured by Teledyne-Hastings Raydist were used to provide the gas mixtures of the desired compositions (O_2, CO_2, and Ar) with high precision (±1% full scale). The high purity gases were obtained from Matheson Gas Products and the traces of water were removed by passing the blended gas through a column of 5Å molecular sieves and Drierite (Fisher Scientific). The gas mixture was bubbled into the melt in the vicinity of the working electrode at a flow rate of 50 cm^3 min^{-1} by a long alumina tube with four holes. The composition of the gas mixture supplied to the reference electrode compartment was the same as the one used for the working electrode, but at a flow rate of 5 cm^3 min^{-1}. The equilibrium between the gas and the carbonate melt was achieved by bubbling the gas for at least 12 h prior to the experiment. For this study, P_{O_2} was varied from 0.1 to 0.8 atm, while P_{CO_2} was kept constant at 0.2 atm. The total pressure was kept constant at 1 atm by varying the partial pressure of argon. The Puratronic grade (99.999%) lithium carbonate (Alfa Products) was carefully weighed in an alumina crucible (90 ml capacity) and the electrochemical cell was slowly heated (50°C/h) to 350°C under inert environment. The electrochemical cell assembly was dried at 350°C in a carbon dioxide environment for 24 h before heating to 800°C. The data acquisition setup consisted of a potentiostat/galvanostat (Model 273), lock-in-amplifier (Model 5301A), personal computer (IBM PS/2), and software (Model 378) supplied by PAR.

Results and Discussion

Cyclic voltammetry.—Cyclic voltammetry measurements were made for oxygen reduction on a gold electrode in a quiescent Li_2CO_3 melt as a function of scan rate, temperature, and P_{O_2}. The working electrode potential was scanned between the rest potential and −0.5V *vs.* reference electrode; the scan rate was varied from 10 to 200 mV/s. The effect of P_{O_2} on the cyclic voltammogram, recorded at the scan rate of 100 mV/s at 800°C temperature is shown in Fig. 1. During the forward scan, a diffusion-limited peak, followed by a limiting plateau, was observed. The peak potential (E_p) was found to be independent of the scan rate (up to 200 mV/s) and the position of this peak was

* Electrochemical Society Student Member.
** Electrochemical Society Active Member.

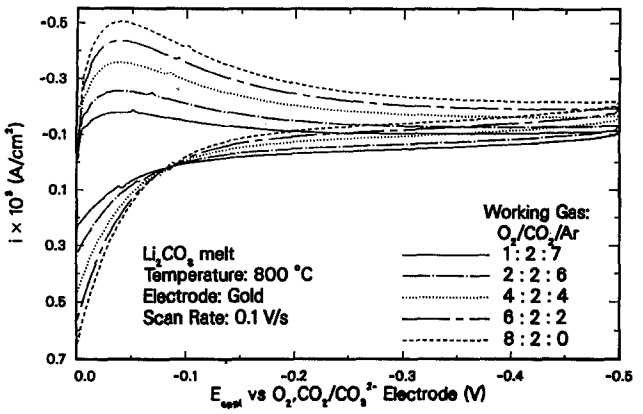

Fig. 1. Effect of P_{O_2} on cyclic voltammogram for O_2 reduction; reference and working gases have the same composition.

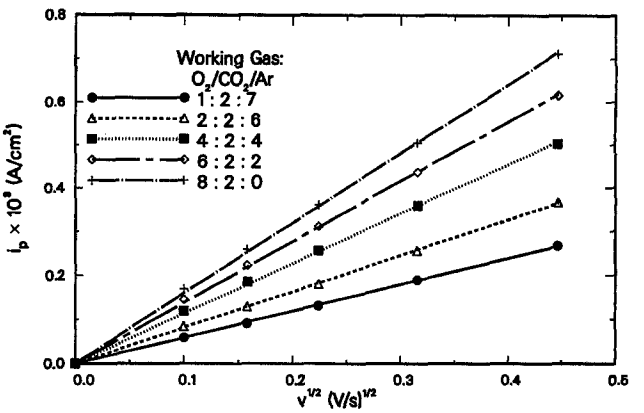

Fig. 2. Effect of P_{O_2} on i_p vs. $v^{1/2}$ plot for O_2 reduction on gold electrode in Li_2CO_3 melt at 0.2 atm P_{CO_2} and 800°C; symbols: experimental data; lines: regression data.

40-45 mV negative to the rest potential. Appleby and Nicholson (2) made a similar observation and attributed it to peroxide reduction in a Li_2CO_3 melt as shown in step [2] of this proposed mechanism

$$1/2\ O_2 + CO_3^{2-} \rightleftharpoons O_2^{2-} + CO_2 \quad [1]$$

$$O_2^{2-} + e^- \rightleftharpoons (O^-) + O^{2-} \quad [2]$$

$$(O^-) + CO_2 + e \rightleftharpoons CO_3^{2-} \quad [3]$$

$$(O^{2-}) + CO_2 \rightleftharpoons CO_3^{2-} \quad [4]$$

$$1/2\ O_2 + CO_2 + 2e^- \rightleftharpoons CO_3^{2-} \quad [5]$$

The small spikes that occur after the peaks are not understood at this time. The current densities in the reverse scan were lower than those in the forward scan and at the end of the cycle, large anodic current densities, which subsided slowly and reached zero in a few minutes, were observed. Lu (5) observed similar behavior for O_2 reduction in Li-K melt and attributed it to an increase in the basicity of the melt near the working electrode due to an accumulation of oxide ions produced during the forward sweep which shifts the equilibrium potential in the negative direction.

A plot of the effect of P_{O_2} on the peak current density (i_p) *vs.* square root of the scan rate ($v^{1/2}$) at 800°C is shown in Fig. 2. The linear behavior of i_p *vs.* $v^{1/2}$, shown in Fig. 2, and invariance of E_p with respect to the scan rate (Fig. 1) indicate that oxygen reduction in a Li_2CO_3 melt is reversible up to 200 mV/s (11). As shown in Fig. 2, an increase in partial pressure of oxygen increased the slope of i_p *vs.* $v^{1/2}$ plot. As suggested by Appleby and Nicholson (2), the diffusion-limited peak for O_2 reduction in Li_2CO_3 can be described by the theory developed by Berzins and Delahay (12) for the reversible diffusion-controlled peak where the product activity is considered to be invariant and equal to unity (*e.g.*, metal deposition). According to Berzins and Delahay, the peak current density is given by the following expression

$$i_p = 0.61(nF/RT)^{1/2}nFD_O^{1/2}C_O v^{1/2} \quad [6]$$

The transport parameter $D_O^{1/2}C_O$ was calculated from the slope of i_p *vs.* $v^{1/2}$ plot using Eq. [6]. The calculated values of the transport parameter for various P_{O_2} are given in Table I. The increase in the partial pressure of oxygen increased the product $D_O^{1/2}C_O$, mainly due to increase in peroxide ion concentration. Plots of the effect of P_{O_2} on the cyclic voltammogram and on the i_p *vs.* $v^{1/2}$ plots at 850°C are shown in Fig. 3 and 4, respectively; estimated values of $D_O^{1/2}C_O$ are given in Table I. The temperature change caused a two-fold increase in $D_O^{1/2}C_O$. Reaction order plots for $D_O^{1/2}C_O$ with respect to P_{O_2}, at constant P_{CO_2}, are shown in Fig. 5. The O_2 reaction order obtained by linear regression analysis is close to +0.5, which agrees well with the peroxide formation step (Eq. [1]) in the reaction mechanism described earlier.

Impedance measurements and analysis.—The impedance measurements were carried out for oxygen reduction in Li_2CO_3 melt at the rest potential as a function of P_{O_2}, temperature, and frequency (0.05 Hz-10 kHz). For frequencies higher than 10 kHz, an inductive behavior (positive imaginary impedance) was observed; hence the high-frequency measurements were limited to 10 kHz. Figures 6 and 7 show the effect of P_{O_2} on the Bode plot (phase angle *vs.* log ω) for 800 and 850°C, respectively. For high frequencies, the phase angle approached 0°, indicating a purely resistive behavior of the impedance. The impedance at 0° phase angle is a measure of the solution resistance (R_s) between the working and reference electrodes. At low frequencies, the phase angle approached −45°, indicating that mass-transfer (Warburg) impedance was dominant. The effect of P_{O_2} on oxygen reduction kinetics is evident at intermediate frequencies, reflecting increased charge-transfer resistance (R_{ct}) with decrease in P_{O_2}. The effect of temperature can be observed by comparison of Fig. 6 and 7; an increase in the temperature decreased the charge-transfer resistance and the mass-transfer resistance became dominant at relatively higher frequencies. The sharp deviations in the data near 110 Hz frequency are due to the measurement system.

A complex nonlinear least squares (CNLS) parameter estimation program (13, 14) based on the Randles-Ershler equivalent circuit (15, 16) was used for the impedance analysis. This analysis provides estimates of the charge-

Table I. Comparison of product $D_O^{1/2}C_O$ estimated by cyclic voltammetry and electrochemical impedance spectroscopy at 0.2 atm P_{CO_2}.

Temperature (°C)	$D_O^{1/2}C_O \times 10^9$ mol cm^{-2} s$^{1/2}$			
	800		850	
P_{O_2} (atm)	Cyclic voltammetry	Impedance analysis	Cyclic voltammetry	Impedance analysis
0.1	1.08	1.03 ± 0.04	2.41	2.53 ± 0.06
0.2	1.49	1.49 ± 0.03	3.71	3.08 ± 0.09
0.4	2.07	2.12 ± 0.07	4.95	5.25 ± 0.17
0.6	2.53	2.70 ± 0.09	6.12	6.60 ± 0.22
0.8	2.92	3.08 ± 0.10	7.26	7.65 ± 0.28

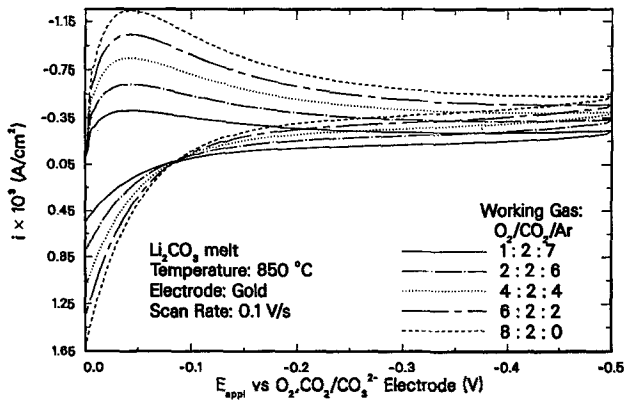

Fig. 3. Effect of P_{O_2} on cyclic voltammogram for O_2 reduction; reference and working gases have same composition.

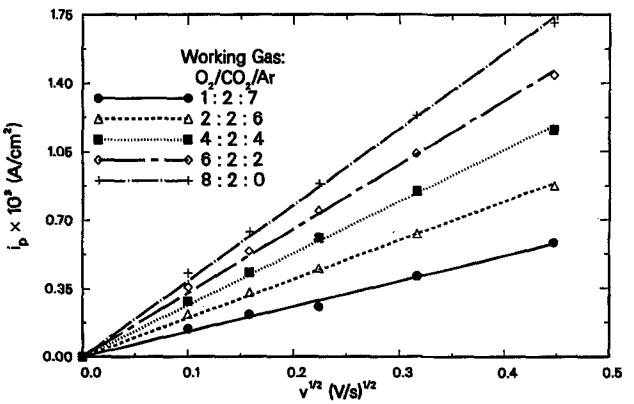

Fig. 4. Effect of P_{O_2} on i_p vs. $v^{1/2}$ plot for O_2 reduction on gold electrode in Li_2CO_3 melt at 0.2 atm P_{CO_2} and 850°C; symbols: experimental data; lines: regression data.

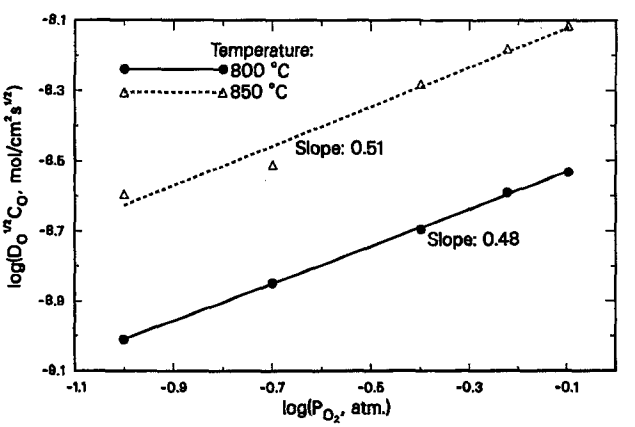

Fig. 5. Plots of log ($D_O^{1/2}C_O$) vs. log (P_{O_2}) for O_2 reaction orders determination at 0.2 atm P_{CO_2}; $D_O^{1/2}C_O$ estimated by cyclic voltammetry.

transfer resistance (R_{ct}), double layer capacity (C_{dl}), Warburg coefficient (σ), and solution resistance (R_s). In our analysis, we found that the weighting factor (inverse of the error variance) influences the accuracy of the parameters estimated from the impedance data. Here, we have used the proportional weighting factor (17) to estimate kinetic and mass-transfer parameters from the impedance data. Figures 8 and 9 show the effect of P_{O_2} on real impedance (Z') *vs.* the inverse square root of angular frequency ($\omega^{-1/2}$) for temperatures 800 and 850°C, respectively. In a low frequency region, Z' *vs.* $\omega^{-1/2}$ plots showed a linear behavior with a slope proportional to the Warburg coefficient (σ). As shown in Fig. 8 and 9, σ decreased with increase in P_{O_2} and temperature, due to an increase in peroxide ion concentration. The curve lines in Fig. 8 and 9 show Z' *vs.* $\omega^{-1/2}$ plots

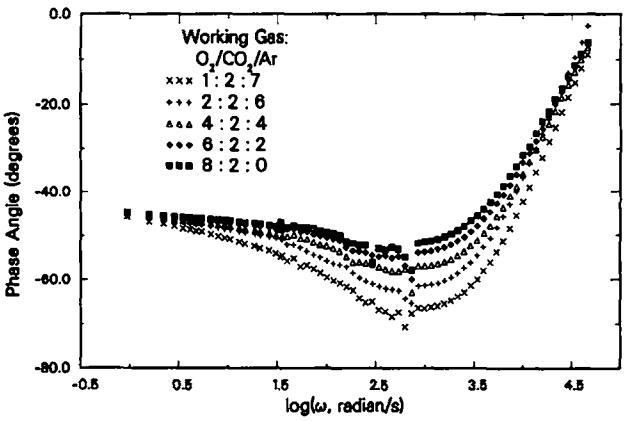

Fig. 6. Phase angle vs. log ω plot as a function of P_{O_2} for O_2 reduction on gold electrode in Li_2CO_3 melt at 0.2 atm P_{CO_2} and 800°C.

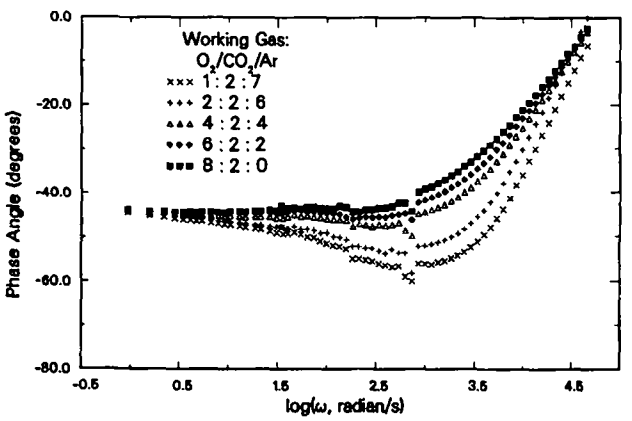

Fig. 7. Phase angle vs. log ω plot as a function of P_{O_2} for O_2 reduction on gold electrode in Li_2CO_3 melt at 0.2 atm P_{CO_2} and 850°C.

for the data computed by the model using estimated parameters. The estimated parameters for various partial pressures of oxygen are given in Tables II and III. These tables show that increase in P_{O_2} and temperature decreased R_{ct} and σ, whereas the change in R_s was negligible. The effects of P_{O_2} and temperature on the impedance spectrum can be observed from log |Z| *vs.* log ω plots shown in Fig. 10 and 11.

Since impedance measurements were obtained at the rest potential, the following expressions can be used for the charge-transfer resistance and the Warburg coefficient (18)

$$R_{ct} = \frac{RT}{nFi_0} \quad [7]$$

$$\sigma = \frac{RT}{n^2F^2A\sqrt{2}}\left(\frac{1}{D_O^{1/2}C_O} + \frac{1}{D_R^{1/2}C_R}\right) \quad [8]$$

For peroxide reduction in Li_2CO_3 melt, C_O is much smaller than C_R because the final product is carbonate ion. Therefore $1/D_R^{1/2}C_R$ is negligible compared with $1/D_O^{1/2}C_O$. Thus Eq. [8] can be approximated by the following expression

$$\sigma = \frac{RT}{n^2F^2A\sqrt{2}}\left(\frac{1}{D_O^{1/2}C_O}\right) \quad [9]$$

Using Eq. [7] (where n = 2, for peroxide reduction), exchange current densities (i_0) calculated for several values of P_{O_2} and temperature, are shown in Tables II and III. The estimated values of the exchange current density are closer to those obtained by Lu (5) and Uchida *et al.* (8) but two-orders of magnitude higher than those observed by Appleby and Nicholson (2) who used the potential sweep technique. Lu used the potential sweep and potential step

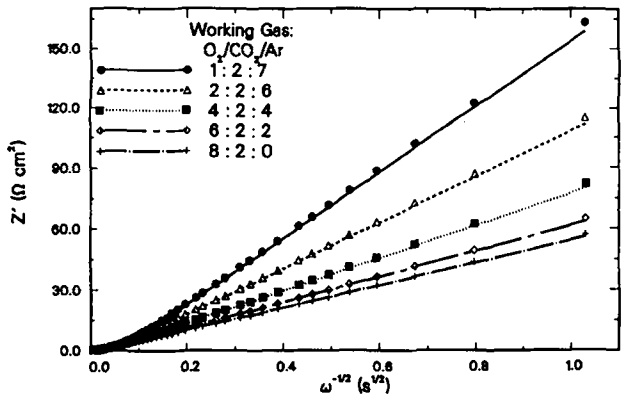

Fig. 8. Effect of P_{O_2} on Z' vs. $\omega^{-1/2}$ plot for O_2 reduction on gold electrode in Li_2CO_3 melt at 0.2 atm P_{CO_2} and 800°C; symbols: experimental data; lines: regression data.

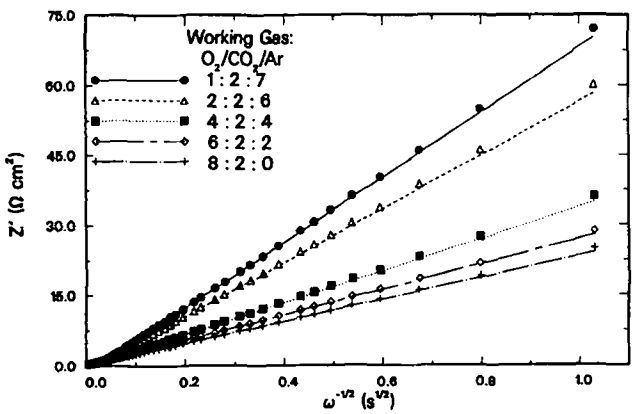

Fig. 9. Effect of P_{O_2} on Z' vs. $\omega^{-1/2}$ plot for O_2 reduction on gold electrode in Li_2CO_3 melt at 0.2 atm P_{CO_2} and 850°C; symbols: experimental data; lines: regression data.

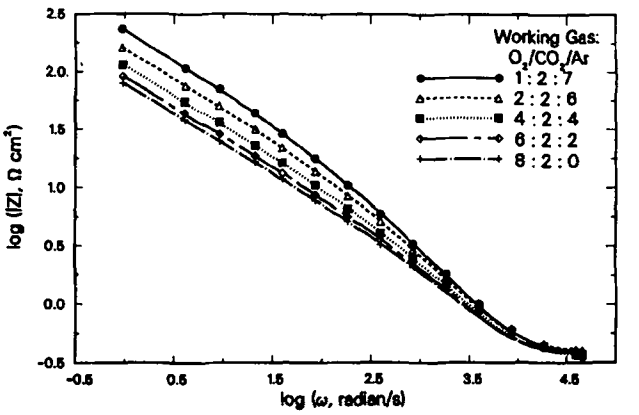

Fig. 10. Effect of P_{O_2} on log |Z| vs. log ω plot for O_2 reduction on gold electrode in Li_2CO_3 melt at 0.2 atm P_{CO_2} and 800°C; symbols: experimental data; lines: regression data.

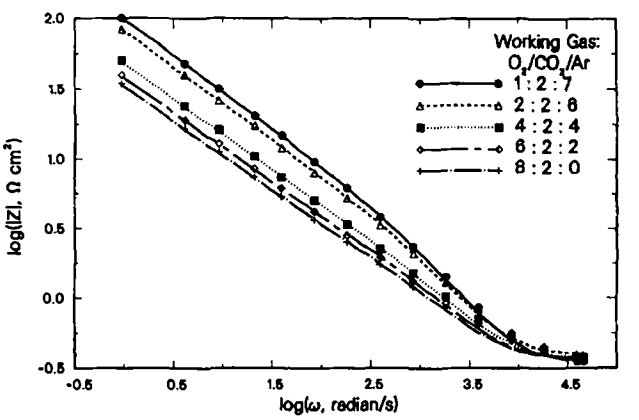

Fig. 11. Effect of P_{O_2} on log |Z| vs. log ω plot for O_2 reduction on gold electrode in Li_2CO_3 melt at 0.2 atm P_{CO_2} and 850°C; symbols: experimental data; lines: regression data.

techniques to study the oxygen reduction in a Li-K (62 m/o:38 m/o) carbonate eutectic mixture on a gold electrode. He showed that the exchange current densities determined by the potential sweep method underestimated the actual values. The plots of exchange current density as a function of the partial pressure of oxygen at two temperatures are shown in Fig. 12. From the slopes of these lines, the reaction orders for oxygen were calculated. At 800°C, the exchange current density yields a positive reaction order of value 0.30 with respect to P_{O_2}, which is consistent with the peroxide reaction mechanism proposed by Appleby and Nicholson (2), when the first charge transfer (Eq. [2]) is the rate determining step (rds) and the symmetry factor (β) has a value of 0.5. As shown in Tables II and III, the capacitance value increased with an increase in P_{O_2} and this increase was more noticeable at higher temperature. The mass-transfer parameter $D_O^{1/2}C_O$ was calculated from the expression for the Warburg coefficient (Eq. [9]). As shown in Table I, the mass-transfer parameters estimated by impedance analysis and cyclic voltammetry techniques are in good agreement. For comparison with

Table II. Electrode kinetic and mass-transfer related parameters estimated by electrochemical impedance spectroscopic technique at 800°C temperature and 0.2 atm P_{CO_2}.

P_{O_2} (atm)	σ (Ω cm² $s^{-1/2}$)	R_{ct} (Ω cm²)	$i_0 \times 10^3$ (A cm^{-2})	$C_{dl} \times 10^6$ (F cm^{-2})	R_s (Ω cm²)
0.1	164.4 ± 6.3	1.79 ± 1.47	25.9 ± 21.3	270.5 ± 14.7	0.35
0.2	114.0 ± 2.5	1.49 ± 0.57	31.1 ± 11.9	292.6 ± 11.0	0.40
0.4	79.8 ± 2.7	1.17 ± 0.52	39.3 ± 17.3	324.3 ± 17.5	0.36
0.6	62.8 ± 2.1	1.07 ± 0.39	43.3 ± 15.7	348.8 ± 18.3	0.37
0.8	55.1 ± 1.9	0.95 ± 0.34	48.7 ± 17.3	366.0 ± 20.8	0.37

Table III. Electrode kinetic and mass-transfer related parameters estimated by electrochemical impedance spectroscopic technique at 850°C temperature and 0.2 atm P_{CO_2}.

P_{O_2} (atm)	σ (Ω cm² $s^{-1/2}$)	R_{ct} (Ω cm²)	$i_0 \times 10^3$ (A cm^{-2})	$C_{dl} \times 10^6$ (F cm^{-2})	R_s (Ω cm²)
0.1	70.1 ± 1.8	1.17 ± 0.35	41.4 ± 11.7	335.9 ± 14.1	0.35
0.2	57.7 ± 1.6	1.06 ± 0.32	45.7 ± 13.2	381.3 ± 18.8	0.39
0.4	33.8 ± 1.1	0.64 ± 0.19	76.0 ± 21.6	485.0 ± 28.8	0.38
0.6	26.9 ± 0.9	0.57 ± 0.15	85.4 ± 21.7	549.8 ± 33.5	0.37
0.8	23.2 ± 0.8	0.50 ± 0.15	96.2 ± 26.7	615.2 ± 41.9	0.37

Table IV. Comparison of the peroxide concentration determined from $D_O^{1/2}C_O$ values (for $D_O = 1 \times 10^{-5}$ cm^2 s^{-1}) with literature values and thermodynamic data at 800°C temperature and 0.2 atm P_{CO_2}.

P_{O_2} (atm)	$C_O \times 10^7$ (mol cm^{-3}) Electrochemical impedance spectroscopy	Ramaswami (20)	Appleby and Van Drunen (19)	Thermodynamic data (21)
0.1	3.41	3.50	2.90	0.72
0.2	4.71	4.95	4.10	1.02
0.4	6.55	7.00	5.80	1.44
0.6	8.53	8.57	7.10	1.76
0.8	9.74	9.89	8.20	2.03

Table V. The reaction order with respect to oxygen for the exchange current density and $D_O^{1/2}/C_O$ estimated by cyclic voltammetric and electrochemical impedance spectroscopic techniques.

Parameter	Technique	Temperature (°C)	Estimated O_2 reaction order	Theoretical O_2 reaction order
$D_O^{1/2}C_O$	Electrochemical impedance spectroscopy	800	0.53 ± 0.02	0.50
		850	0.56 ± 0.11	
	Cyclic voltammetry	800	0.48 ± 0.01	
		850	0.51 ± 0.07	
i_0	Electrochemical impedance spectroscopy	800	0.30 ± 0.03	0.38
		850	0.44 ± 0.18	

the data available in literature, the concentration of peroxide (C_O) was calculated from the mass-transfer parameter $D_O^{1/2}C_O$ for the diffusion coefficient of about 1×10^{-5} cm^2 s^{-1}. As shown in Table IV, the estimated concentrations of peroxide compared well with those determined from the oxygen solubility measurements of Appleby and Van Drunen (19) and Ramaswami (20). The theoretical values of peroxide concentration in pure lithium carbonate melt estimated from thermodynamic data (21) were much smaller than those determined by experiment. The discrepancy between the theoretical and experimental data is due to large uncertainty involved with the thermodynamic data for the molten alkali carbonates. The plots to determine reaction order with respect to oxygen for the product $D_O^{1/2}C_O$ are shown in Fig. 13. The reaction orders obtained are consistent with those obtained from cyclic voltammetric measurements. As demonstrated in Table V, the oxygen reaction orders for the peroxide formation and the exchange current density for oxygen reduction determined by cyclic voltammetric and electrochemical impedance spectroscopic techniques are compared well with the theoretical values.

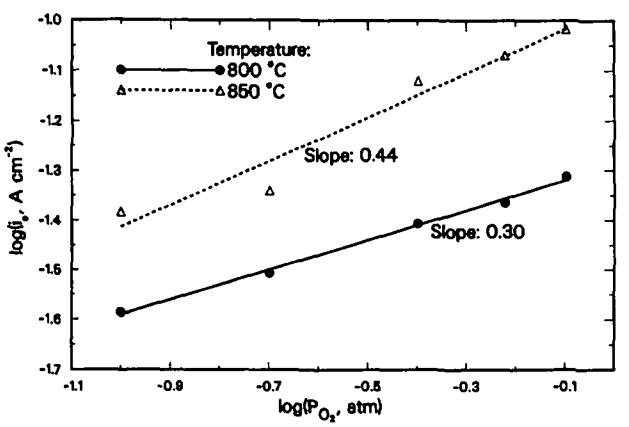

Fig. 12. Plots of log i_0 vs. log P_{O_2} for O_2 reaction orders determination at 0.2 atm P_{CO_2}; symbols: experimental data; lines: regression data.

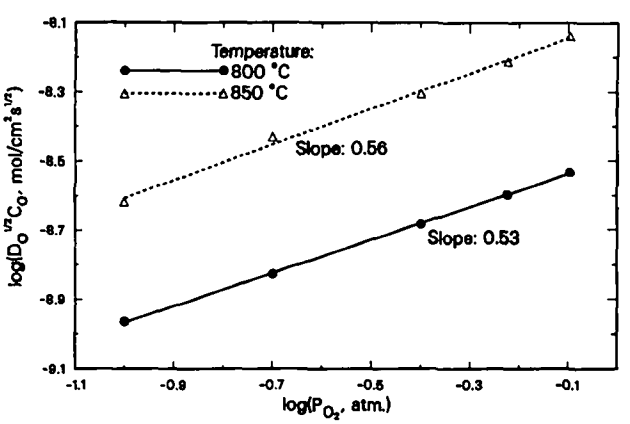

Fig. 13. Plots of log ($D_O^{1/2}C_O$) vs. log (P_{O_2}) for O_2 reaction orders determination at 0.2 atm P_{CO_2}; $D_O^{1/2}C_O$ estimated by impedance analysis.

Conclusions

The kinetic and mass-transfer related parameters for the oxygen reduction in pure Li_2CO_3 were determined as a function of P_{O_2} and temperature by impedance analysis. The transport parameter $D_O^{1/2}C_O$, obtained by both impedance analysis and by cyclic voltammetry, showed excellent agreement. The oxygen reaction orders resulting from the mass-transfer parameters and the exchange current densities at 800°C were determined to be 0.5 and 0.30, respectively. These values are consistent with the peroxide reduction mechanism proposed by Appleby and Nicholson.

Acknowledgments

Financial support for this project from the U.S. Department of Energy (Contract No. DE-FG22-87PC79931) and Electric Power Research Institute (Contract No. RP8002-7) is gratefully acknowledged.

Manuscript submitted April 16, 1990; revised manuscript received Sept. 25, 1990.

Texas A&M University assisted in meeting the publication costs of this article.

LIST OF SYMBOLS

A	electrode area, cm^2
C_{dl}	double layer capacitance, F/cm^2
C_j	bulk concentration of species j, mol/cm^3
D_j	bulk diffusion coefficient of species j, cm^2/s
E_p	peak potential, V
F	Faraday's constant, 96,487 C/equiv.
i	current density, A/cm^2
i_0	exchange current density, A/cm^2
i_p	peak current density, A/cm^2

n number of electrons transferred in electrode reaction
R universal gas constant, 8.314 J/mol · K
R_{ct} charge-transfer resistance, Ω cm²
R_s solution resistance, Ω cm²
T temperature, K
v scan rate, V/s
Z overall impedance, Ω cm²
Z' real part of impedance, Ω cm²
Z'' imaginary part of impedance, Ω cm²
$|Z|$ modulus of impedance, Ω cm²

Greek

β symmetry factor for electrochemical reaction
σ Warburg coefficient, Ω cm² $s^{-1/2}$
ω angular frequency, radian/s

Subscripts

O peroxide ions
R carbonate ions

REFERENCES

1. A. J. Appleby and S. B. Nicholson, *J. Electroanal. Chem.*, **38,** App. 13 (1972).
2. A. J. Appleby and S. B. Nicholson, *ibid.*, **53,** 105 (1974).
3. A. J. Appleby and S. B. Nicholson, *ibid.*, **83,** 309 (1977).
4. A. J. Appleby and S. B. Nicholson, *ibid.*, **112,** 71 (1980).
5. S. H. Lu, Ph.D. Dissertation, Illinois Institute of Technology, Chicago, IL (1985).
6. I. Uchida, T. Nishina, Y. Mugikura, and K. Itaya, *J. Electroanal. Chem.*, **206,** 229 (1986).
7. I. Uchida, Y. Mugikura, T. Nishina, and K. Itaya, *ibid.*, **206,** 241 (1986).
8. I. Uchida, T. Nishina, Y. Mugikura, and K. Itaya, *ibid.*, **209,** 125 (1986).
9. B. B. Davé, Ph.D. Dissertation, Texas A&M University, College Station, TX (1990).
10. T. Nishina, M. Takahashi, and I. Uchida, *This Journal*, **137,** 1112 (1990).
11. R. S. Nicholson and I. Shain, *Anal. Chem.*, **36,** 706 (1964).
12. T. Berzins and P. Delahay, *J. Am. Chem. Soc.*, **75,** 555 (1953).
13. J. R. Macdonald, *J. Electroanal. Chem.*, **223,** 25 (1987).
14. J. R. Macdonald, in "Impedance Spectroscopy," J. R. Macdonald, Editor, p. 1, John Wiley & Sons, New York (1987).
15. J. E. B. Randles, *Discuss. Faraday Soc.*, **1,** 11 (1947).
16. B. Ershler, *ibid.*, **1,** 269 (1947).
17. J. R. Macdonald and L. D. Potter, Jr., *Solid State Ionics*, **23,** 61 (1987).
18. M. Sluyters-Rehbach and J. H. Sluyters, in "Electroanalytical Chemistry," Vol. 4, A. J. Bard, Editor, p. 1, Marcel Dekker, Inc., New York (1970).
19. A. J. Appleby and C. Van Drunen, *This Journal*, **127,** 1655 (1980).
20. K. Ramaswami, Ph.D. Dissertation, Illinois Institute of Technology, Chicago, IL (1990).
21. B. Kr. Andersen, Ph.D. Dissertation, The Technical University of Denmark, Lyngby, Denmark (1975).

The Behavior of Zinc Electrode in Alkaline Electrolytes

I. A Kinetic Analysis of Cathodic Deposition

C. Cachet, B. Saïdani, and R. Wiart

UPR 15 du CNRS "Physique des Liquides et Electrochimie," Laboratoire de l'Université Pierre et Marie Curie, 75252 Paris Cédex 05, France

ABSTRACT

A model for the cathodic electrode activation is developed so as to account for the polarization curves and impedance plots obtained for zinc deposition in alkaline electrolytes. The reaction pattern involves the two-step discharge of zincate ions through an oxide-containing layer whose ionic and electronic conductivities are potential activated. The sharp electrode activation with increasing cathodic polarization is shown to be related to the spreading and thinning of the conductive layer. These phenomena and the concentration of the monovalent intermediate in the layer account for the three time-constants distinguished in the inductive electrode impedance. The growth of granular compact deposits, favored by trace lead in the electrolyte, is associated with the existence of a uniformly conductive layer on the whole electrode surface. The presence of a fluorinated surfactant (F1110) inhibits the formation of spongy deposits in close connection with modifications to both the kinetic parameters of reactions and the geometrical parameters of the conductive layer.

Zinc deposition is known to occur mainly from zincate ions $Zn(OH)_4^{2-}$ (1-3) but the structure of zincate complexes in supersaturated alkaline electrolytes is not yet completely established. Recent results obtained with concentrated solutions by laser Raman and ^{67}Zn NMR methods have concluded in favor of the symmetrical tetrahedral form $Zn(OH)_4^{2-}$ (4). The latest data from spectroscopic techniques, EXAFS and neutron diffraction, do not reveal any difference between under- and supersaturated solutions, and they have been explained by considering the presence of waters of hydration around the $Zn(OH)_4^{2}$ ion (5, 6). Thus, the species responsible for supersaturation would be different from the main tetrahydroxozincates by the number of water molecules (5).

On the other hand the kinetics and the reaction mechanism of the deposition and dissolution of zinc in alkaline solutions are still a matter for discussion. A controversy exists about the reaction mechanisms which have been derived from the values of reaction orders, Tafel slopes, and exchange current densities deduced from short-time transient measurements (7-14), the quantitative data concerning these parameters being spread over a rather wide range of values. Dirkse and Hampson (7, 8) proposed the following mechanism

$$Zn + OH^- \leftrightarrows Zn\,OH^- \quad [D\text{-}1]$$

$$Zn\,OH^- \rightarrow Zn\,OH + e \quad [D\text{-}2]$$

$$Zn\,OH + OH \leftrightarrows Zn(OH)_2 + e^- \quad [D\text{-}3]$$

$$Zn(OH)_2 + 2\,OH^- \leftrightarrows Zn(OH)_4^{2-} \quad [D\text{-}4]$$

in which the rate-determining step for zinc dissolution is the electrochemical reaction [D-2], in agreement with the exchange current density observed to be independent of the zincate concentration. Later on, Dirkse pointed out that the zinc electrode behavior is sensitive to the ionic strength in the electrolyte, and from comparisons at constant ionic strength, he confirmed that the rate-determining step occurs early in the anodic sequence (9).

A second mechanism was proposed by Bockris *et al.* (10)

$$Zn + OH^- \leftrightarrows Zn\,OH + e^- \quad [B\text{-}1]$$

$$Zn\,OH + OH^- \leftrightarrows Zn(OH)_2 \quad [B\text{-}2]$$